Heterogeneous and Monolithic 3D Integrated Full-Color Micro-Light-Emitting Diodes via CMOS-Compatible Oxide Bonding for µLEDoS

Hyun soo Kim, Juhyuk Park, Woo Jin Baek, Dae-Myeong Geum, Inki Kim, Hyeongrak Lim, Jinha Lim, Seong Kwang Kim, Jaeyong Jeong, Joonsup Shim, Jung Hong Min, and Sang Hyeon Kim*

Micro-light emitting diode (µLED) based LED on silicon (LEDoS) is a promising candidate for next-generation AR and VR displays due to superior pixel performance and potential for high resolution. Traditional RGB pixels are placed on a single plane, which limits the resolution. To overcome this, vertically stacked RGB pixels using heterogeneous and monolithic 3D integration (M3D) have been explored. However, previously reported vertical µLED pixels have not considered the heat dissipation capability of the pixels, which is indeed important in future micro displays, and utilized materials incompatible with standard CMOS processes, further limiting their practicality for LEDoS. The critical regions for constraint, the bonding medium, are typically organic polymer materials. Therefore, to handle issue, vertically stacked full-color µLEDs are demonstrated using silicon oxide (SiO_2) and yttrium oxide (Y_2O_3), as bonding mediums. These materials are CMOS-compatible and offer thermal conductivity at least 10 times higher than conventional polymers. The InGaN/GaN blue µLEDs bonded with oxides show improved thermal management, leading to higher external quantum efficiency (EQE) and better color characteristics, including narrower full width at half maximum (FWHM) and higher color purity. Precise control over bonding layer thickness is achieved, minimizing pixel thickness and enhancing manufacturability for high-resolution displays.

1. Introduction

Recent advancements in display technology have focused on providing users with immersive experiences in virtual environments through near-eye head-mounted displays. Attributes such as ultra-high resolution, high brightness, and precise color accuracy are essential to achieve exceptional viewing experiences in extended reality (XR) devices, including AR and VR glasses. Among potential solutions, micro light-emitting-diode (µLED) based LED on silicon (LEDoS) has emerged as a promising candidate, offering the necessary specifications for next-generation displays.[1–7]

To realize near-eye display-oriented LEDoS, the LEDoS display must achieve high resolution, low power consumption, and low operation temperature in the display module perspective. However, the conventional transfer method of µLED pixels limits achieving high resolution. The conventional transfer method involves the mechanical transfer of

H. soo Kim, J. Park, W. J. Baek, I. Kim, H. Lim, J. Lim, S. K. Kim, J. Jeong, J. Shim, S. H. Kim
School of Electrical Engineering
Korea Advanced Institute of Science and Technology
Daejeon 34141, Republic of Korea
E-mail: shkim.ee@kaist.ac.kr

D.-M. Geum
School of Electronics Engineering
Inha University
Incheon 22212, Republic of Korea

J. H. Min
Photonic Semiconductor Research Center
Korea Photonics Technology Institute
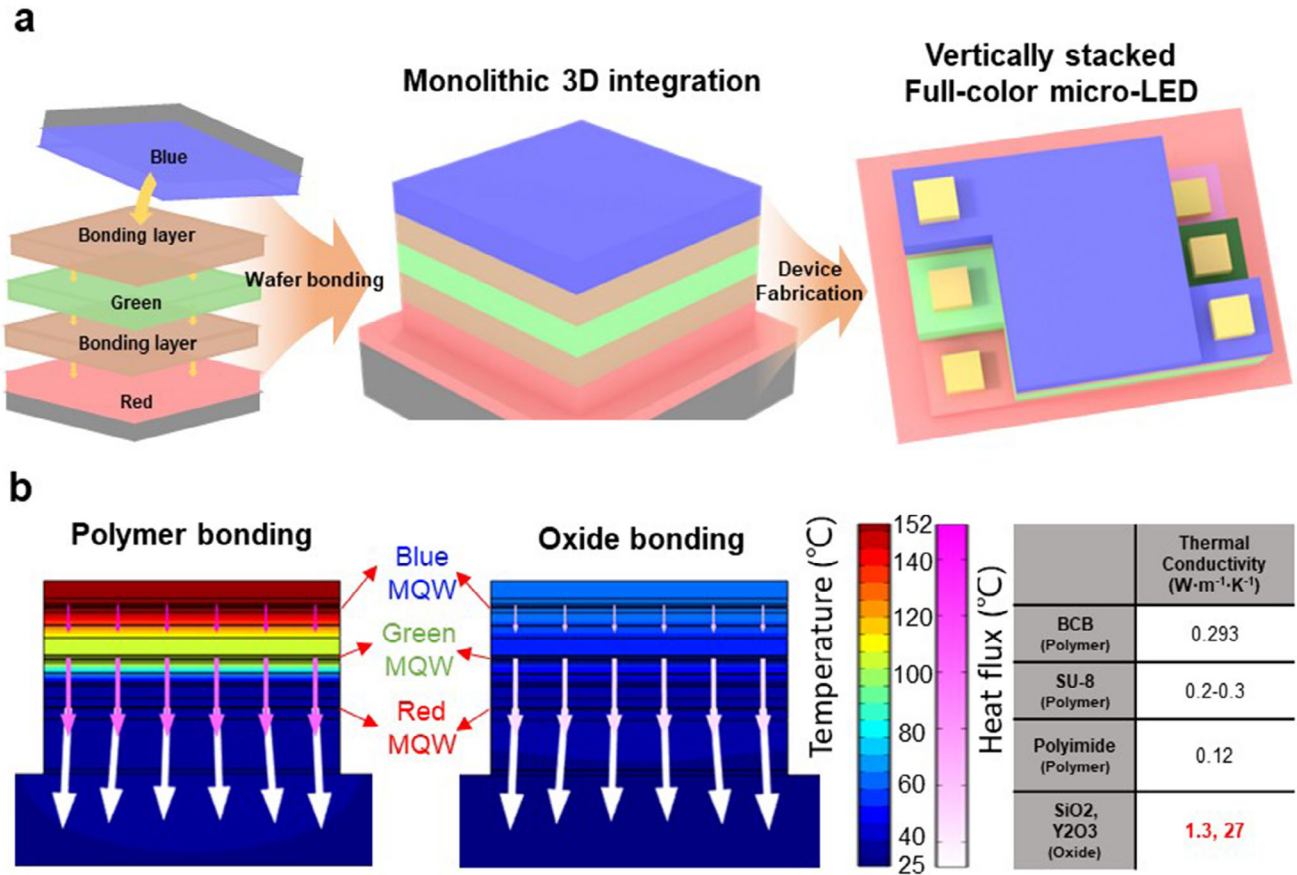Gwangju 61007, Republic of Korea

Figure 1. Schematic of vertically stacked full-color μLED with 3 different wafer bonding layer components (BCB, SiO$_2$, Y$_2$O$_3$). a) Fabrication process of vertically stacked full-color μLED. b) Thermal comparison of polymer bonding and oxide bonding via heat simulation.

individual sub-pixels to the CMOS wafer, making precise placement at micrometer scale challenging due to the limited mechanical alignment accuracy, and thus limiting the display resolution that must be achieved for near-eye display.[8,9]

Heterogeneous and monolithic 3D integration (HM3D) addresses these limitations by stacking diverse heterogenous epitaxy layers (R, G, B) and sequentially fabricating full-color μLEDs, as illustrated in **Figure 1a**.[10–21] The sequential process integration of HM3D enables denser integration by the vertical arrangement of the sub-pixels and lithographic alignment, enabling the achievement of over twice the high pixels per inch (PPI), compared to mechanical alignment in conventional mass transfer.[10]

However, self-heating of the pixels can be the limitation in the vertically stacked pixels.[22] Considering that these devices are aimed at near-eye LEDoS, which must have low operating power and temperature, the advantages in resolution of vertically stacked pixels can be deteriorated due to the self-heating of the device. The increased temperature of the LED due to self-heating induces higher non-radiative recombination, resulting in degradation of external quantum efficiency (EQE) and power consumption efficiency. Furthermore, the increased temperature of the pixels can induce red shift in the emission wavelength due to bandgap narrowing, distorting color reproduction during display operation.[23]

In this study, we first demonstrate a vertically stacked full-color μLED utilizing an oxide bonding medium selected for its process suitability and heat dissipation capability. This approach shows superior CMOS compatibility and enhanced heat dissipation properties, highlighting the potential of this method for advanced display applications. As shown in Figure 1b,[24–27] simulations comparing temperature variations under the vertically stacked full-color μLED structure with the same power dissipation indicate that oxide bonding achieves more effective heat sinking to the substrate, resulting in a lower junction temperature. Additionally, to clarify the appropriate bonding layer for vertically stacked full-color μLED, we fabricated InGaN/GaN-based μLEDs with different bonding layers: Oxide bonding [Silicon oxide (SiO$_2$) / Yttrium oxide (Y$_2$O$_3$) / SiO$_2$] and polymer [Benzocyclobutene (BCB)] layers and systematically compared the electrical, optical, and thermal characteristics of devices. Based on the comparative analysis, our device fabricated with oxide bonding showed the highest color purity and narrowest full width at half maximum (FWHM) among reported 3D stacked full-color μLEDs. We believe that the technologies described in this study will serve as significant milestones and standards for vertically stacked μLEDs toward the realization of future ultra-high resolution displays.
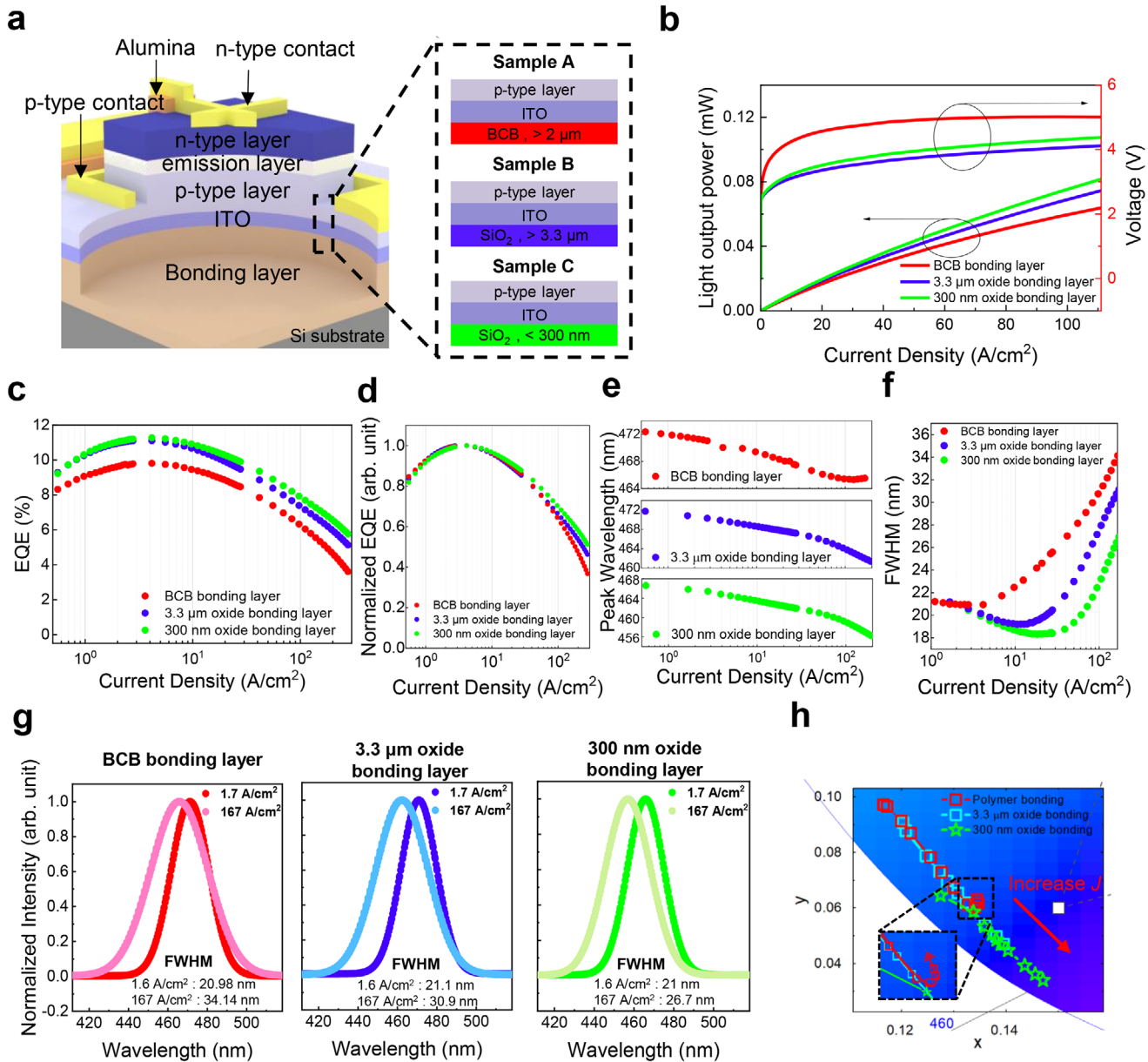
ADVANCED
SCIENCE NEWS
www.advancedsciencenews.com

LASER
& PHOTONICS
REVIEWS

www.lpr-journal.org

Figure 2. Electrical and Optical characteristics of µLEDs with 3 types of bonding layer (BCB, 3.3 µm SiO$_2$ + Y$_2$O$_3$, 300 nm SiO$_2$ + Y$_2$O$_3$). a) Schematic of a µLED constructed with three types of bonding layers. Sample A: BCB bonding layer, Sample B: 3.3 µm oxide bonding layer, and Sample C: 300 nm oxide bonding layer. b) Light output power-current density and voltage-current density curves of Sample A, B, and C. c) EQE-logarithmic current density curve. d) Normalized EQE-logarithmic current density curve from maximum EQE to 300 A cm^{-2} e) Peak wavelength-logarithmic current density curve. f) FWHM depending on current density. g) EL spectra of Sample A, B, and C at 1.6 and 167 A cm^{-2} (The EL spectra were extracted through Gaussian fitting). h) Color coordinate of Sample A, B, and C with increasing current density (red arrow direction means increasing current density).

2. Comparison of µLED Device Characteristics Based on Polymer and Oxide Bonding Layer

The thermal-related coefficients vary depending on the bonding material, significantly impacting overall performance of the µLEDoS display. To compare the effects of bonding materials, Sample A employed a BCB polymer bonding layer with a thickness of ≈2 µm, while Samples B and C utilized oxide bonding layers with different thicknesses. As illustrated in **Figure** 2a, three types of bonding layers were used to fabricate InGaN/GaN-based blue µLEDs on Si substrates. The oxide bonding layers consist of stacked structures of SiO$_2$ and Y$_2$O$_3$, where Y$_2$O$_3$ serves as a bonding interface with a total thickness of <20 nm. Although Samples B and C used the same bonding materials, their bonding layer thicknesses differed: Sample B has a 3.3 µm-thick bonding layer, while Sample C has a 300 nm-thick layer. The vertical stacking of red, green, and blue LEDs inherently increases the overall device thickness, as it adds up the thickness of active layers for each color LEDs and the intermediate bonding layers. This increased device thickness presents challenges in HM3D-based display fab-

rication technology, particularly in photolithography and mesa structures etching processes. Polymer bonding layers made with BCB generally result in relatively thick layers due to the spin coating process, making precise thickness control more challenging. In contrast, SiO_2 bonding layers enable precise thickness control and can be fabricated ultra-thin through deposition and chemical mechanical polishing (CMP) processes. Therefore, three distinct samples were fabricated to systematically evaluate the impact of bonding layer materials and thicknesses.

The light output power-current density (L-I) and voltage-current density (V-J) characteristics of Sample A, B, and C, for $60 \times 60 \ \mu m^2$ µLED, are shown in Figure 2b. The light output power increases linearly with current density, and the continuous output across all regions confirms effective carrier injection and emission. Furthermore, Sample C (300 nm oxide bonding) exhibits the highest light output power across all current densities. Figure 2c presents the EQE for µLEDs, with different bonding layers, where the device size is $60 \times 60 \ \mu m^2$. The maximum efficiencies of Samples A, B, and C were recorded as 9.8%, 11.1%, and 11.3%, respectively. The polymer bonding in Sample A resulted in slight lower efficiency compared to the oxide bonding in Sample B and C. The difference can be attributed to internal quantum efficiency (IQE) and light extraction efficiency (LEE).[28]

IQE degradation due to thermal effects can be observed.

IQE can be represented by the ABC + $f(n)$ model,

$$IQE = \frac{Bn^2}{An + Bn^2 + f(n)} \tag{1}$$

where A and B are the coefficients for Shockley-Read-Hall (SRH) recombination and radiative recombination. The $f(n)$, which includes the term Cn^3 (C is Auger coefficient), relates to non-radiative recombination mechanisms, such as leakage and n is the carrier concentration. As the temperature increases, SRH recombination rises, primarily influenced by impurities and defects. Simultaneously, the contribution of the "$f(n)$" term increases, leading to enhanced carrier leakage and a reduction in radiative efficiency. These two mechanisms contribute to the decreased IQE of LEDs at high temperatures.[29] The impact of the heat generation during the LED operation can be observed in Figure 2d,e. Figure 2d illustrates the normalized EQE graph. The normalized EQE graph shows that: starting at 50 A cm^{-2}, Sample A's droop begins to exceed that of the other two samples, and as the current density increases, the droop becomes even steeper. (We calculated the EQE droop ratio for each sample in Figure S4 (Supporting Information), and Sample C exhibits the overall lowest droop ratio.) This suggests that in Sample A, the EQE decreases more sharply in the high current density region due to increased Auger recombination caused by self-heating.[30] Additionally, Figure 2e illustrates the peak wavelengths of the emission spectra for each sample with $60 \times 60 \ \mu m^2$ µLED, as a function of current density. Typically, in InGaN/GaN-based LEDs, the peak wavelength shift is influenced by two factors. First, an increased carrier injection leads to a blue shift in the electroluminescence (EL) peak due to the quantum confined Stark effect (QCSE).[31,32] Second, rising temperature from self-heating in µLEDs induces bandgap narrowing, causing a red shift in the peak wavelength.[33,34] As shown in Figure 2e, with increasing current density, the peak wavelengths of Sample B and C shift to-

ward blue, indicating the dominance of QCSE. In contrast, Sample A shows a different trend compared to the other two samples. Above 100 A cm^{-2}, the red shift becomes more dominant than the blue shift. This indicates that in Sample A, the red shift caused by significant heat generation surpasses the conventional blue shift observed at higher injection. In other words, the results showed that Sample A generated more heat compared to Sample B and C. Overall, Figure 2d,e confirms that as current density increases, enhanced heat generation leads to a thermally dominated effect on both the EQE and peak wavelength shift.

LEE is influenced by the structure of the device and optical factors such as the absorption and reflectance of the layers that make up the device. These factors play a crucial role in light extraction efficiency, and the LEE can vary significantly depending on the characteristics of bonding layer (In this study, all aspects are identical except for the composition of the bonding layer). Unlike the SiO_2 layer in oxide bonding, the BCB layer used in polymer bonding absorbs ≈30%, resulting in an overall reduction in LEE (The absorption and LEE simulation is summarized in Figures S5–S7, Supporting Information).[35] The peak wavelength shift can alter the refractive index and absorption of the bonding layer, thereby affecting LEE. Additionally, as the thickness of the bonding layer increases, Fabry-Pérot resonance induces multiple reflections within the layer, leading to interference effects at specific wavelengths and subsequent variations in reflectance. However, the impact of these factors on LEE is relatively minor compared to the changes caused by absorption in the bonding layer.

In summary, the EQE differences observed in Figure 2c can be attributed to two main factors. First, due to absorption in the BCB bonding layer, Sample A exhibits lower LEE compared to Samples B and C. Second, the self-heating effect contributes to the difference. As shown in the IQE plot in Figure S8 (Supporting Information), the IQE difference due to self-heating increases with higher current density, which leads to a larger EQE difference. Additionally, the minor EQE difference in IQE-comparable region is influenced by minor LEE variations caused by wavelength shifts and changes in reflectance.

To achieve precise and vivid color representation in high-resolution displays, a narrow FWHM and high color purity are essential. Figure 2f illustrates the FWHM of each sample as a function of current density for µLED with a size of $60 \times 60 \ \mu m^2$. The FWHM of all three samples tends to increase with higher current density due to the band filling effect.[36] However, FWHM differs between the samples, increasing in the order of Sample C, Sample B, and Sample A. As mentioned earlier, Sample A potentially generates the greatest amount of heat. When the temperature rises, lattice vibrations and electron-phonon interactions intensify, leading to energy level broadening. This results in EL peak broadening and an increase in FWHM.[37] Consequently, Sample A exhibits the broadest FWHM, as confirmed in Figure 2g. At 1.6 A cm^{-2}, all samples have a similar FWHM values. However, at 167 A cm^{-2}, Sample A exhibits the broadest spectrum with minimal peak shift, attributed to a red shift by heat (The EL spectra at other current densities are provided in Figure S3, Supporting Information). The color coordinates corresponding to different current densities are plotted in Figure 2h within the CIE 1931 color space (As current density increases from 1 to 167 A cm^{-2}, the coordinates shift in the direction indicated by the red arrows). In Sample A, bending toward the green coordinate first
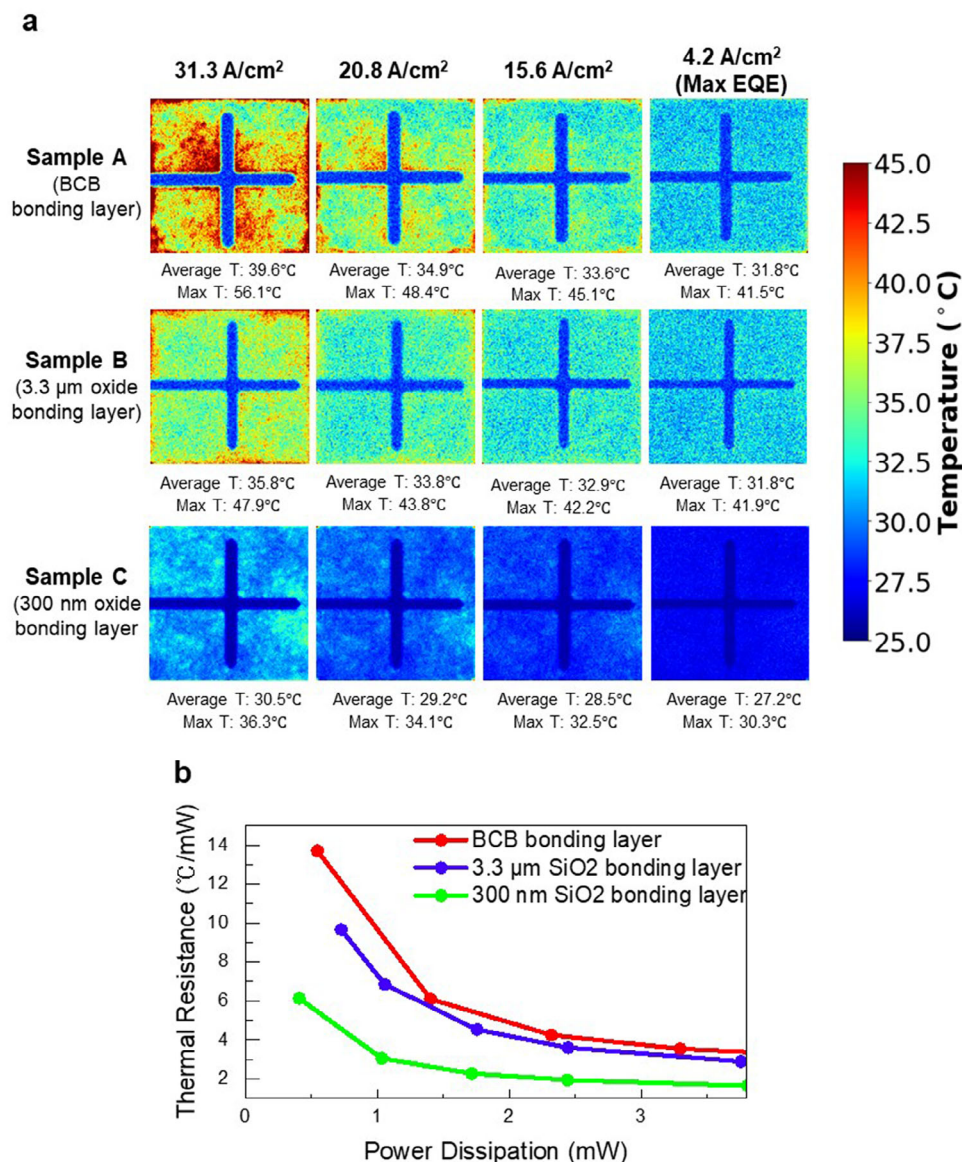
Figure 3. Measurement of device temperature of sample A, B, and C. a) 2D thermal profile, which measured at four different current densities. b) Thermal resistance-power dissipation curve.

occurs at 100 A cm^{-2}, which coincides with the red shift point in Figure 2e. This bending in the CIE 1931 causes the color coordinates to deviate from the dominant wavelength, leading to color purity degradation at higher current densities (Figure S9, Supporting Information presents the color purity of each sample). Additionally, a comparison of the displayable color gamut, using the same red and green coordinates, reveals that this bending reduces the color gamut.

3. Heat Characteristics of μLED Devices Depending on the Bonding Layer

Thus far, we have confirmed heat generation in each sample by observing its impact on EQE, emitting wavelength, and color purity. Notably, the impact varied with the type of bonding

layer used. In this section, we employed CCD-based thermal reflectance microscopy (TRM) to intuitively measure heat generation and to analyze the actual heat dissipation behaviors of the samples.[38–40] Thermal measurements were performed on devices with a size of 60×60 μm^2 and different bonding layers, across various current densities, as shown in **Figure 3a**. At low current injection of 4.2 A cm^{-2}, Sample A and B (thick oxide bonding layer) showed almost similar thermal mapping images with an average temperature of 31.8 °C. However, as the current density increases to 31.3 A cm^{-2}, Sample A exhibited more extensive red mapping data across the entire mesa area, indicating a higher temperature. Specifically, the average temperatures of samples A and B are 39.6 and 35.8 °C, respectively, while their maximum temperatures reached 56.1 and 47.9 °C. Sample A exhibited a higher temperature across the whole mesa area. This

**ADVANCED
SCIENCE NEWS**

www.advancedsciencenews.com

**LASER
& PHOTONICS
REVIEWS**

www.lpr-journal.org

higher temperature and nonuniformity would impact the emitting behaviors, which was shown as a large FWHM of EL spectra. In contrast, sample C consistently shows the lowest temperature across all current density ranges, with its maximum temperature ≈20 °C lower than sample A at 31.3 A cm^{-2}. These results suggest the oxide bonding layers dissipate heat much effectively than polymer bonding layers, a finding that aligns with the red shift trends in the peak wavelength observed in Figure 2. By analyzing the average temperature change and power extracted at each current density, we calculated thermal resistance, as shown in Figure 3b. Thermal resistance represents the degree to which a material resists heat transfer, and increases with the material's thickness.[41] Consistently, Sample C exhibited lower thermal resistance than Sample B across all power dissipation levels. Lower thermal resistance indicates better heat dissipation, suggesting that Sample C can maintain high performance at elevated current densities without suffering from efficiency degradation, reduced lifespan, or color shift due to thermal effects. From the analysis of TRM measurement data, we identified two key factors that influence the temperature differences between samples. The first factor is the thermal conductivity of the bonding layer. For example, BCB has a thermal conductivity about one-fourth that of SiO$_2$, causing it to retain more heat and leading to higher temperatures in Sample A compared to Samples B and C. The other factor is the thickness of the bonding layer, which affects thermal properties even for the same bonding material.

4. Demonstration of Vertically Stacked Full-Color μLED with Oxide Bonding Layer

In the previous sections, we clearly identified several advantages of using oxide bonding layers rather than conventional polymer-based bonding layers. These advantages include minimizing reductions in IQE caused by thermal effects, reducing LEE loss due to absorption, and maintaining high color quality, which are critical for ultra-high-resolution display applications. Consequently, we introduced oxide materials for the bonding layer in forming full-color pixels and successfully demonstrated the vertically stacked full-color μLED. The transmission electron microscope (TEM) images are shown in **Figure** 4a. From the TEM images and the selected area diffraction (SAED) pattern obtained, we confirmed that the red, blue, and green epitaxy layers were successfully bonded without any defects/voids and exhibited high crystallinity demonstrating excellent structural integrity. The success of the bonding is attributed to the wafer bonding technique, which preserves the quality of each epitaxial layer without damage during the bonding process. The electrical and optical characteristics of the fabricated full-color μLED are presented in Figure S13 (Supporting Information). The turn-on voltages determined from the linear J-V curve plot were 2.75, 2.64, and 2.83 V for the red, green, and blue μLED, respectively. The maximum EQE of vertically stacked full-color μLEDs were 0.42%, 0.62%, and 8.4% for the red, green, and blue, respectively. Here, we have not much considered the LEE in this work, thereby, the EQE seems to be relatively low, but it can be improved in future studies. In the full-color μLEDs, each LED exhibits slightly different device sizes due to the alignment margins inherent in the sequential top-down photolithography process, with dimensions of

57.5 × 57.5, 26.7 × 26.7, 44.1 × 44.1 μm^2 for the red, green, and blue μLED, respectively (Figure S14, Supporting Information). As shown in Figure 4b, our device successfully emitted a full range of colors including yellow, orange, cyan, pink, purple, and white, with the corresponding EL spectra illustrated in Figure 4c. Figure 4d demonstrates the color coordinates of the full-color μLED within the CIE 1931 color space. The CIE 1931 coordinates for red, green, and blue are (0.6964, 0.2939), (0.1171, 0.0762), and (0.2945, 0.6805), respectively. The calculated color purity based on the RGB coordinates is 97.3% for red, 93.2% for green, and 99.2% for blue, with a 94.4% overlap with the DCI-P3 color gamut. The color purity of each R, G, and B component represents the highest values reported to date for full-color μLEDs. In high-resolution displays, such as those used in AR/VR, where pixel density is extremely high, precise color representation and accurate color differentiation are crucial. Therefore, both color purity and FWHM are key factors. Based on the data extracted from Figure 4c,d, we plotted color purity as a function in terms of FWHM including the state-of-the-art vertically stacked full-color μLEDs, presented in Figure 4e and Table S1 (Supporting Information). Among the full-color stacked devices reported to date, each μLEDs in this work achieves the highest color purity and the narrowest-level FWHM. Overall, the red, green, and blue μLEDs demonstrate exceptional color characteristics. We benchmarked the key performance metrics, such as the bonding layers properties, device size, and color characteristics, of reported vertically stacked full-color μLED displays including the device presented in this work,[15–17] as shown in Table S1 (Supporting Information). Our full-color μLED, which utilizes an oxide bonding layer, is demonstrated for the first time compared to all previous works that used polymer bonding and exhibit superior thermal performance, attributed to differences in thermal conductivity. Moreover, it features the superior color characteristics discussed earlier and achieves the highest overlap of 94.4% based on the DCI-P3 color gamut, resulting in more accurate and vivid color reproduction on high-resolution displays.

5. Conclusion

In summary, we have first demonstrated a CMOS-compatible vertically stacked full-color μLED using an oxide bonding layer and HM3D technology for μLEDoS applications. To validate this demonstration, we compared polymer-based and oxide-based bonding by fabricating samples with BCB and SiO$_2$ + Y$_2$O$_3$ bonding layer, respectively, and evaluated their electrical, optical, and thermal properties. The comparison revealed that the oxide bonding samples exhibited an overall higher EQE due to lower LEE degradation and minimized IQE degradation caused by absorption and thermal effects in the BCB bonding layer. Additionally, we observed that the thermal characteristics of oxide bonding layers depends on their thickness, with thicker layers exhibiting increased efficiency degradation at higher current densities due to heat. Using TRM, we measured the device temperature and confirmed that the polymer bonding layer generates significantly more heat than oxide bonding layer. Subsequently, we successfully fabricated a full-color μLED that demonstrated excellent color characteristics.
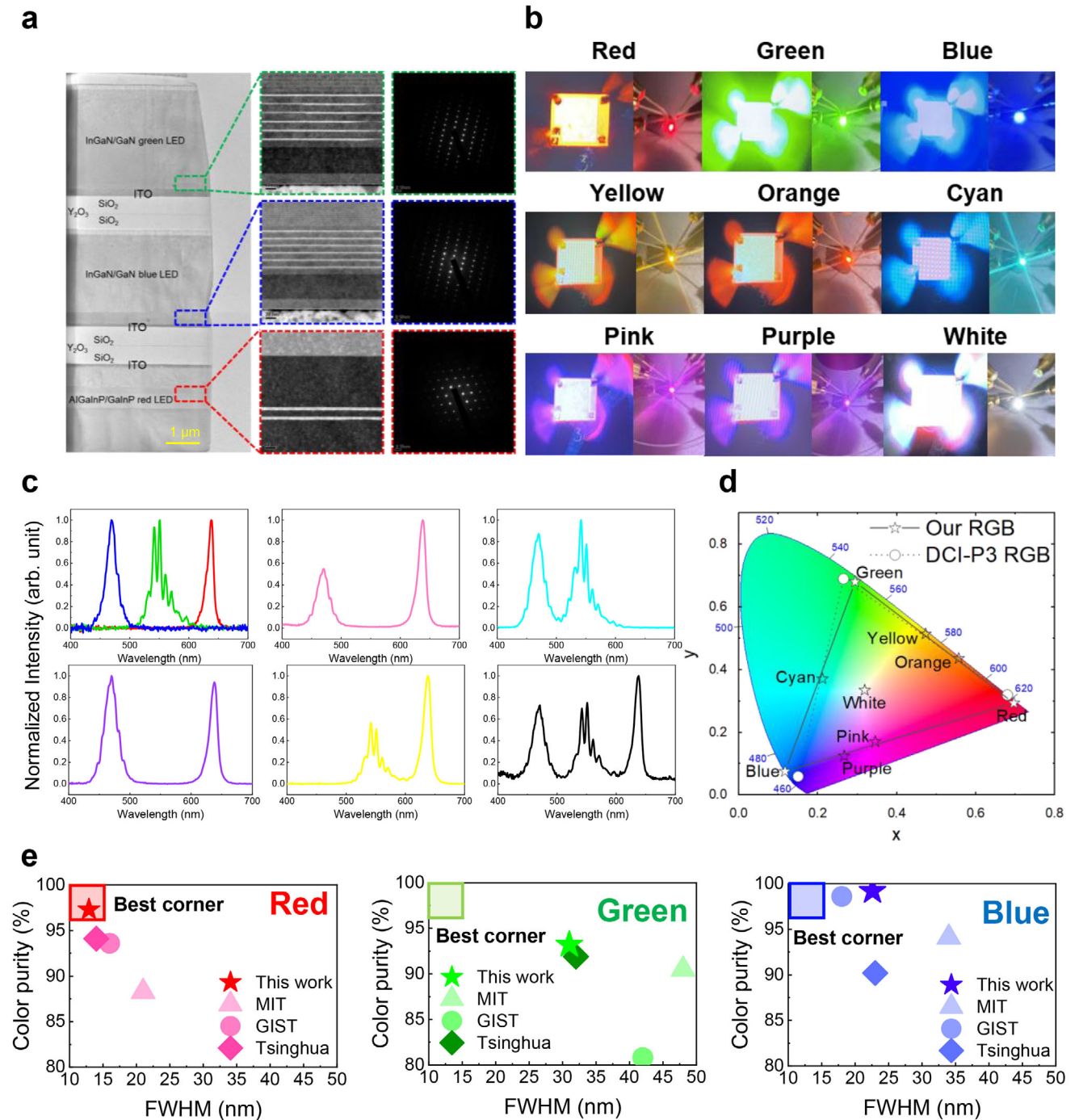
Figure 4. Vertically stacked full-color μLED with oxide bonding layer for μLEDoS display. a) TEM image of vertically stacked red, blue, and green epitaxy layers. b) EL image of full-color μLED showing red, green, blue, yellow, orange, cyan, pink, purple, and white through RGB color mixing. c) EL spectra at each color. d) Color coordinate of μLED in the CIE 1931 color space with DCI-P3(dashed line). e) Comparison of color purity-FWHM plots for each group of full-color μLEDs.

6. Experimental Section/Methods

Epitaxial Growth of InGaN-Based Blue μLED: The nitride-based blue μLEDs were fabricated using epitaxial wafers grown on 8-inch Si (111) substrates through the process of metal-organic chemical vapor deposition (MOCVD). To mitigate the high defect density and cracking result- ing from the lattice constant mismatch between Si (111) substrates and GaN, a buffer layer was employed. The buffer layer comprises an AlN seed layer, an AlGaN/AlN superlattice, and an AlGaN buffer layer. Following this, Si-doped n-type GaN layers were deposited, succeeded by a 20-pair InGaN/GaN (1.3 nm/2 nm) superlattice for strain relief. This was followed by a 6-pair InGaN/GaN multi quantum wells (MQW) layer with a thick-

ness of 2.7 nm/10.8 nm. The structure of the nitride-based blue µLED was completed with an AlInGaN electron blocking layer and a Mg-doped p-type GaN layer.

Epitaxial Growth of InGaN-Based Green µLED: The structure of the nitride-based green µLED is identical to that of the nitride-based blue µLED, except for the InGaN/GaN superlattice and the MQW layers. The superlattice consists of 32 pairs of InGaN/GaN (5 nm/2 nm), while the MQW layer is composed of InGaN/GaN with thicknesses of 2.7 and 13.5 nm, respectively.

Epitaxial Growth of Phosphide-Based Red µLED: The phosphide-based red µLEDs were grown on a 4-inch GaAs substrate. The overall structure consists of an N+ GaAs buffer layer, an n-type AlGaInP layer, MQW structure, and p-type AlGaInP and GaP layers. The MQW structure was composed of a 7 nm GaInP quantum well and a 14 nm AlGaInP quantum barrier.

Preparation Before Bonding Process: Silicon and nitride-based wafers intended for bonding were first diced into dimensions of 2×2 cm^2 and 1.8×1.8 cm^2, respectively. The diced wafers were then subjected to sequential cleaning using acetone, methanol, and isopropyl alcohol. Following the cleaning process, a 200 nm thick indium tin oxide (ITO) transparent electrode was deposited via electron-beam evaporation. To establish the ohmic contact, the nitride-based blue LED was annealed at 550 °C for 5 min in an air-ambient environment.

SiO$_2$ Bonding Process: SiO$_2$ was deposited on a nitride-based wafer using plasma enhanced chemical vapor deposition (PECVD) at 400 °C. To achieve oxide bonding, it is essential to maintain a root mean square (RMS) surface roughness of <1 nm across the epi surfaces to ensure uniform bonding without voids. However, atomic force microscopy (AFM) measurements revealed that the RMS value of the SiO$_2$ layer deposited via PECVD exceeded 1 nm. Therefore, CMP was employed to achieve the necessary surface roughness. Subsequently, Y$_2$O$_3$ was deposited via sputtering, and bonding was carried out using heat and pressure.

BCB Bonding Process: A layer of BCB was applied onto Si wafer pieces via spin coating. Following the coating process, the samples were prebaked at 150 °C for 10 min. The BCB-coated Si substrate was then placed in a bonder, and a nitride-based blue LED intended for bonding was positioned on top. After establishing a vacuum, the pressure was gradually increased to 2–4 kg cm^{-2}. The temperature was then ramped up at a rate of 10 °C min^{-1} to 150 °C, where the sample was baked for 10 min. Subsequently, the temperature was further increased to 250 °C at a rate of 5 °C min^{-1}, and bonding was performed for 1 h at 250 °C. After the bonding process, the temperature was gradually reduced, and once ambient temperature was reached, the bonded sample was removed from the bonder.[42]

Full-Color µLED Bonding Process: To fabricate a full-color vertically stacked µLED, nitride-based blue and green LEDs, along with a phosphide-based red LED, were prepared. The epitaxial wafers were diced into 2 cm × 2 cm sections, followed by sequential cleaning using acetone, methanol, and isopropyl alcohol. A 200 nm thick ITO transparent electrode was deposited via electron-beam evaporation. For ohmic contact formation, the nitride-based blue and green LEDs were annealed at 550 °C for 5 min in an air ambient environment, while the phosphide-based red LED underwent annealing at 200 °C and 200 mTorr for 5 min. Subsequently, a SiO$_2$ bonding layer was deposited using PECVD. The surface roughness was minimized to an RMS value below 1 nm via CMP. Y$_2$O$_3$ was then sputter-deposited, and thermal compression bonding was performed under heat and pressure. The silicon substrate was removed through dry etching, and due to the etching selectivity between the n-GaN buffer layer and the silicon substrate, etching was stopped at the n-GaN buffer layer. Afterward, an additional SiO$_2$ bonding layer was deposited on the red and blue bonding samples, followed by CMP to achieve the required surface roughness. The green LED was then bonded in a similar manner, and the silicon substrate was removed using the same process. Mesa structures for the red, green, and blue LEDs were formed using inductively coupled plasma reactive ion etching (ICP-RIE). Finally, aluminum oxide (Al$_2$O$_3$) was deposited using atomic layer deposition (ALD), and contact metal areas were defined on each mesa. Metal electrodes were deposited via electron-beam evaporation, completing the fabrication of the full-color µLED.[43]

Measurement Method: The electrical characteristics of the devices were measured using a Keysight B1500A. The optical properties were extracted by calibrating data measured with a 4-inch integrating sphere, an optical spectrum analyzer, and a silicon photodiode connected to the Keysight B1500A. The chromaticity was determined based on EL spectra and color coordinates obtained from the integrating sphere and optical spectrum analyzer. To quantitatively analyze the thermal profile of the µLEDs at specific current densities, TRM was employed. A 2 Hz voltage pulse was applied using a Keithley 4200, while images were captured at a 30 Hz frame rate over 10 s. To eliminate reflectance changes due to optical emission from the µLEDs, a bandpass filter with a central wavelength of 661 nm (FWHM ~10 nm) was used in the light input path, and a 660 nm (FWHM ~10 nm) filter was placed in front of the CCD camera (Pco Edge 4.2 LT) to ensure that only reflectance changes due to thermal effects were observed. The thermal reflectance coefficient was calculated by measuring the average reflectance change in the mesa region of the device as the temperature was incrementally increased from room temperature.

Simulation: The absorption of BCB bonding layer was investigated using rigorous coupled-wave analysis (RCWA). The simulated structure and environment were configured to be identical to those of the actual device in this work. The *n* and *k* values of the BCB material were extracted based on transmission and reflection measurements. Additionally, the LEE simulation for each sample was carried out using a 3D finite-difference time-domain (FDTD) simulation program by Lumerical Inc.

Supporting Information

Supporting Information is available from the Wiley Online Library or from the author.

Acknowledgements

Conflict of Interest

The authors declare no conflict of interest.

Data Availability Statement

The data that support the findings of this study are available from the corresponding author upon reasonable request.

Keywords

[1] V. W. Lee, N. Twu, I. Kymissis, *Inform. Display* **2016**, *32*, 16.
[2] E. L. Hsiang, Z. Yang, Q. Yang, Y. F. Lan, S. T. Wu, *J. Soc. Inform. Display* **2021**, *29*, 446.

[3] S.-H. Kim, S.-K. Kim, J.-P. Shim, D.-M. Geum, G. Ju, H.-S. Kim, H.-J. Lim, H.-R. Lim, J.-H. Han, S. Lee, *IEEE J. Electron Devices Soc.* **2018**, *6*, 579.

[4] J. Park, D.-M. Geum, W. Baek, J. Shieh, S. Kim, Symposium on VLSI Technology and Circuits, **2022**, 383 384.

[5] J. Park, E.-J. Youn, W. J. Baek, E.-K. Chu, H. S. Kim, D.-M. Geum, J. P. Kim, B. H. Kim, S.-H. Kuk, H.-H. Park, *Opt. Express* **2024**, *32*, 24242.

[6] Z. Chen, S. Yan, C. Danesh, *J. Phys. D: Appl. Phys.* **2021**, *54*, 123001.

[7] W. J. Baek, J. Park, J. Shim, B. H. Kim, S. Park, H. S. Kim, D.-M. Geum, S. H. Kim, *Nat. Commun.* **2023**, *14*, 1386.

[8] S.-I. Park, Y. Xiong, R.-H. Kim, P. Elvikis, M. Meitl, D.-H. Kim, J. Wu, J. Yoon, C.-J. Yu, Z. Liu, *Science* **2009**, *325*, 977.

[9] J. Day, J. Li, D. Lie, C. Bradford, J. Lin, H. Jiang, *Appl. Phys. Lett.* **2011**, *99*, 031116.

[10] D.-M. Geum, S. K. Kim, C.-M. Kang, S.-H. Moon, J. Kyhm, J. Han, D.-S. Lee, S. Kim, *Nanoscale* **2019**, *11*, 23139.

[11] C.-M. Kang, S.-J. Kang, S.-H. Mun, S.-Y. Choi, J.-H. Min, S. Kim, J.-P. Shim, D.-S. Lee, *Sci. Rep.* **2017**, *7*, 1.

[12] C.-M. Kang, D.-J. Kong, J.-P. Shim, S. Kim, S.-B. Choi, J.-Y. Lee, J.-H. Min, D.-J. Seo, S.-Y. Choi, D.-S. Lee, *Opt. Express* **2017**, *25*, 2489.

[13] C.-M. Kang, J.-Y. Lee, D.-J. Kong, J.-P. Shim, S. Kim, S.-H. Mun, S.-Y. Choi, M.-D. Park, J. Kim, D.-S. Lee, *ACS Photonics* **2018**, *5*, 4413.

[14] J. Chun, K. J. Lee, Y.-C. Leem, W.-M. Kang, T. Jeong, J. H. Baek, H. J. Lee, B.-J. Kim, S.-J. Park, *ACS Appl. Mater. Interfaces* **2014**, *6*, 19482.

[15] L. Li, G. Tang, Z. Shi, H. Ding, C. Liu, D. Cheng, Q. Zhang, L. Yin, Z. Yao, L. Duan, *Proc. Natl. Acad. Sci. U. S. A.* **2021**, *118*, 2023436118.

[16] J. Shin, H. Kim, S. Sundaram, J. Jeong, B.-I. Park, C. S. Chang, J. Choi, T. Kim, M. Saravanapavanantham, K. Lu, *Nature* **2023**, *614*, 81.

[17] S. H. Mun, C. M. Kang, J. H. Min, S. Y. Choi, W. L. Jeong, G. G. Kim, J. S. Lee, K. P. Kim, H. C. Ko, D. S. Lee, *Adv. Mater. Interfaces* **2021**, *8*, 2100300.

[18] K. Hui, X. Wang, Z. Li, P. Lai, H. Choi, *Opt. Express* **2009**, *17*, 9873.

[19] H. S. El-Ghoroury, Z. Y. Alpaslan, **2014**, in: *Proc. of The Int. Display Workshops*, 1298–1295.

[20] H. Choi, K. N. Hui, X. Wang, Semiconductor color-tunable broadband light sources and full-color microdisplays, US7982228B2, **2010**.

[21] H. S. El-Ghoroury, R. G. W. Brown, D. A. McNeill, H. DenBoer, A. J. Lanzone, Quantum photonic imagers and methods of fabrication thereof, US7623560B2, **2009**.

[22] J. Jeong, S. K. Kim, J. Kim, D.-M. Geum, S. Kim, **2022**, in IEEE Electron Devices Technology & Manufacturing Conference (EDTM), pp. 79–81.

[23] D.-P. Han, D.-G. Zheng, C.-H. Oh, H. Kim, J.-I. Shim, D.-S. Shin, K.-S. Kim, *Appl. Phys. Lett.* **2014**, *104*, 151108.

[24] S. Callard, G. Tallarida, A. Borghesi, L. Zanotti, *J. Non-Cryst. Solids* **1999**, *245*, 203.

[25] P. H. Klein, W. J. Croft, *J. Appl. Phys.* **1967**, *38*, 1603.

[26] S. Erfantalab, G. Parish, A. Keating, *Int. J. Heat Mass Transfer* **2022**, *184*, 122346.

[27] D. Chemical, Processing Procedures for CYCLOTENE 4000 Series Photo BCB Resins **2009**, available at: http://www.microchem.com/PDFs_Dow/cyclotene_4000_immersion_dev.pdf (accessed: December 2011).

[28] E. F. Schubert, Light-emitting diodes 3rd ed., Rensselaer Polytechnic Institute Troy, New York, ISBN: 978-0-9 863826-6-6.

[29] D. S. Meyaard, Q. Shan, Q. Dai, J. Cho, E. F. Schubert, M.-H. Kim, C. Sone, *Appl. Phys. Lett.* **2011**, *99*, 221103.

[30] E. Kioupakis, Q. Yan, D. Steiauf, C. G. Van de Walle, *New J. Phys.* **2013**, *15*, 125006.

[31] J.-H. Ryou, P. D. Yoder, J. Liu, Z. Lochner, H. Kim, S. Choi, H. J. Kim, R. D. Dupuis, *IEEE J. Sel. Top. Quantum Electron.* **2009**, *15*, 1080.

[32] T. Takeuchi, S. Sota, M. Katsuragawa, M. Komori, H. Takeuchi, H. A. H. Amano, I. A. I. Akasaki, *Jpn. J. Appl. Phys.* **1997**, *36*, L382.

[33] J. Liu, W.-S. Tam, H. Wong, V. Filip, *Microelectron. Reliability* **2009**, *49*, 38.

[34] X. Shan, Y. Li, H. Yu, R. Lin, C. Tan, R. Wang, Y. Luo, X. Cui, R. Liu, P. Tian, *Opt. Express* **2024**, *32*, 20412.

[35] T.-X. Lee, C.-Y. Lin, S.-H. Ma, C.-C. Sun, *Opt. Express* **2005**, *13*, 4175.

[36] Y. Liu, F. Feng, K. Zhang, F. Jiang, K.-W. Chan, H.-S. Kwok, Z. Liu, *J. Phys. D: Appl. Phys.* **2022**, *55*, 315107.

[37] Y. Liu, B.-R. Hyun, Y. Wang, K. Zhang, H. S. Kwok, Z. Liu, *ACS Appl. Electron. Mater.* **2020**, *3*, 3.

[38] M. Farzaneh, K. Maize, D. Lüerßen, J. Summers, P. Mayer, P. Raad, K. Pipe, A. Shakouri, R. Ram, J. A. Hudgings, *J. Phys. D: Appl. Phys.* **2009**, *42*, 143001.

[39] J. Jeong, S. K. Kim, J. Kim, D.-M. Geum, S. Kim, **2021**, in: IEEE International Electron Devices Meeting (IEDM), P. 11.2. 1-11.2. 4.

[40] J. Shim, J. Lim, D.-M. Geum, J.-B. You, H. Yoon, J. P. Kim, W. J. Baek, J.-H. Han, S. Kim, *IEEE Trans. Electron Devices* **2021**, *69*, 2151.

[41] O. Käding, H. Skurk, K. Goodson, *Appl. Phys. Lett.* **1994**, *65*, 1629.

[42] S. Keyvaninia, M. Muneeb, S. Stanković, P. Van Veldhoven, D. Van Thourhout, G. Roelkens, *Opt. Mater. Express* **2012**, *3*, 35.

[43] J. Park, W. Baek, D.-M. Geum, S. Kim, *Nanoscale Res. Lett.* **2022**, *17*, 29.